OPTICA

High pixel throughput voltage imaging based on repetitive optical selective exposure (ROSE)

Shun Xiong,[1,†] Luxin Peng,[2,†] Lusheng Gu,[3,7] Peng Zou,[2,4,5,8] and Wei Ji[3,6,9]

[1]College of Life Science and Technology, HUAZHONG University of Science and Technology, Hubei, China
[2]College of Chemistry and Molecular Engineering, Peking University, Beijing 100871, China
[3]National Laboratory of Biomacromolecules, CAS Center for Excellence in Biomacromolecules, Institute of Biophysics, Chinese Academy of Sciences, Beijing 100101, China
[4]Synthetic and Functional Biomolecules Center, Beijing National Laboratory for Molecular Sciences, Key Laboratory of Bioorganic Chemistry and Molecular Engineering of Ministry of Education, PKU-IDG/McGovern Institute for Brain Research, Peking-Tsinghua Center for Life Sciences, Peking University, Beijing 100871, China
[5]Chinese Institute for Brain Research (CIBR), Beijing 102206, China
[6]Bioland Laboratory, Guangzhou 510005, China
[7]gulusheng@ibp.ac.cn
[8]zoupeng@pku.edu.cn
[9]jiwei@ibp.ac.cn
[†]These authors contributed equally.

Received 20 February 2025; revised 25 March 2025; accepted 14 April 2025; published 10 June 2025

Biological fluorescence imaging is constrained by a trade-off between field of view (FoV) and acquisition rate. This limitation is particularly evident with scientific complementary metal oxide semiconductor (sCMOS) cameras, where high frame rates force the maximum FoV into a narrow, high aspect ratio rectangle. Moreover, the rolling shutter used in high-speed imaging produces non-uniform exposure across the FoV, introducing artifacts when capturing rapid dynamics such as fast-moving objects or fluctuating fluorescence signals. These issues are especially detrimental to voltage imaging, a key technique for studying nervous system dynamics. Here, we introduce ROSE-based high-speed imaging (ROSE-HSI), a method that increases pixel throughput sixfold (when compared with a square FoV) by selectively exposing two cameras. ROSE-HSI not only overcomes the sampling rate limitations of a single camera but also eliminates the temporal inaccuracies caused by the rolling shutter. Our technique has enabled simultaneous kilohertz voltage imaging over a 700 × 732-pixel area, capturing distinct neuronal waveforms and synaptic-mediated signal propagation with high fidelity.

https://doi.org/10.1364/OPTICA.560101

1. INTRODUCTION

Functional imaging technologies have dramatically advanced over recent decades, emerging as powerful tools for interrogating nervous system dynamics. Among these techniques, voltage imaging stands out for its ability to directly track changes in the membrane potential (V_m), enabling detailed mapping of action potential (AP) and subthreshold activities with high spatial-temporal resolution [1,2]. Taking advantage of the flourishing growth in sensitivity, brightness, and kinetics of genetically encoded voltage indicators (GEVIs) over the past decade, voltage imaging has achieved broad application across cells, tissues, and animals, providing unprecedented throughput and cell specificity [3–7]. Voltage imaging poses stringent demands in terms of acquisition rate, signal-to-noise ratio (SNR), and field of view (FoV). While the sCMOS camera has the capability to meet these requirements, its full potential in pixel throughput remains untapped due to limitations in its readout principle [8]. For example, a typical 16-bit sCMOS camera is always limited to approximately 200 imaging lines (10% of the sCMOS target) at a 1 kHz frame rate, thus restricting the simultaneous recording throughput to the local part of a single neuron (i.e., the soma or few adjacent neurites could be captured at commonly used 4× magnification). Additionally, the rolling shutter mode introduced for high-speed imaging in the sCMOS camera causes asynchronous exposure and readout across the lines in each frame, distorting AP waveforms in voltage imaging [9–11]. While recent studies have attempted to enhance the equivalent FoV and acquisition rate of AP imaging through repetitive acquisition with multiple-round stimulation, these methods often fall short of capturing spontaneous V_m fluctuations [12,13].

2. WORKING PRINCIPLE AND VERIFICATION

Building on our previous work in interferometric single-molecule localization microscopy based on repetitive optical selective exposure (ROSE) [14,15], we herein propose a ROSE-based high-speed imaging (ROSE-HSI) system to enhance the spatial-temporal performance of voltage imaging with sCMOS cameras. The ROSE-HSI technique employs synchronized modulation of laser

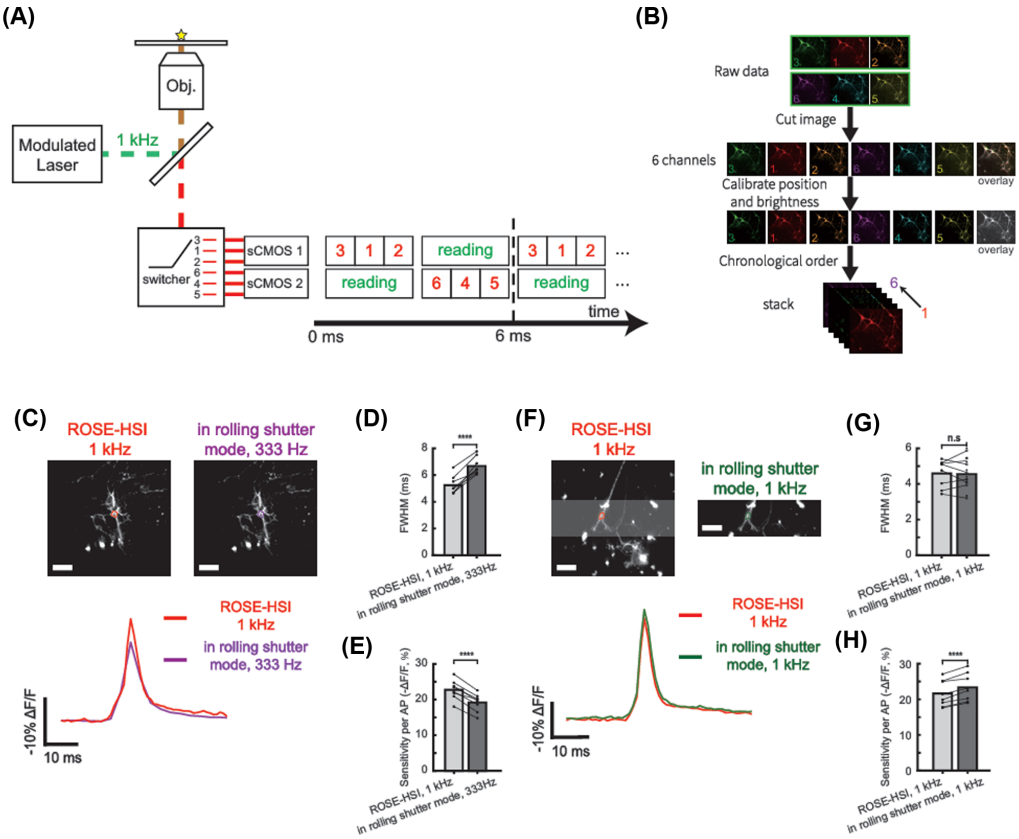

Fig. 1. Scheme and proof-of-concept verification of ROSE-HSI. (A) Working principle of ROSE-HSI. (B) Processing workflow. Brightness correction and registration were applied to six sub-channels to form a temporally ordered stack. (C) Top: comparison of the image of a neuron expressing HVI-AF594 at an identical FoV acquired from ROSE-HSI and conventional wide-field imaging in rolling shutter mode. Bottom: the AP traces averaged from 20 AP signals extracted from the soma at 1 kHz ROSE-HSI (in red) and 333 Hz imaging in rolling shutter mode (in magenta), respectively. Data were acquired with a magnification time of 12.8. Scale bar = 50 μm. (D) and (E) Comparison of APs recorded from 1 kHz ROSE-HSI and 333 Hz imaging in rolling shutter mode on the same neurons ($n = 8$) in FWHM (5.24 ± 0.68 ms versus 6.68 ± 0.66 ms) and sensitivity ($-22.75 \pm 2.71\%$ versus $-19.17 \pm 2.50\%$). Statistical significance was determined by ratio paired t-test. $p^{****} < 0.0001$. (F): Top: images of a neuron expressing HVI-AF594 at the 1 kHz available FoV in ROSE-HSI (left) and imaging in rolling shutter mode (right). Bottom: the AP traces averaged from 20 AP signals extracted from the soma at 1 kHz from ROSE-HSI (in red) and imaging in rolling shutter mode (in green), respectively. Scale bar = 50 μm. (G) and (H) Comparison of APs recorded from 1 kHz ROSE-HSI and imaging in rolling shutter mode on the same neurons ($n = 8$) in FWHM (4.59 ± 0.78 ms versus 4.55 ± 0.85 ms) and sensitivity ($-21.64 \pm 3.66\%$ versus $-23.35 \pm 3.88\%$). Statistical significance was determined by ratio paired t-test. $p^{****} < 0.0001$; n.s., $p > 0.05$.

and galvo mirror-based rapid optical path switching to achieve temporal pixel multiplexing during single-frame camera acquisition [Fig. 1(A)]. The laser excites the genetically encoded voltage indicators (GEVIs), and the fluorescence, channeled through the same objective, is scanned by a one-dimensional galvo mirror, being sequentially swapped among six sub-optical paths pointing to corresponding positions on two sCMOS cameras. The exposure and readout of the two cameras are performed alternately so that the time interval between each sub-image is 1/3 of the exposure duration of each camera, thereby surpassing the sampling limit of the camera. It should be noted that the two sCMOS cameras operate in an external level-triggered global reset mode combined with pulsed illumination, which facilitates the realization of the global shutter function and ensures that the exposure reading times of different horizontal lines are precisely identical (Fig. S1 of Supplement 1). In addition, the alternate use of two cameras avoids the sampling "vacuum period" caused by the reading time of a single camera (Figs. S2 and S3 of Supplement 1). Since the six sub-images inevitably have differences in position or brightness (Fig. S4), registration and background subtraction of each sub-image are necessary before being rearranged into a chronological movie [Fig. 1(B), for details, see Section 5]. We introduced a small initial offset to the signal of the galvo mirror in the actual imaging, so the first captured sub-image is in the middle of the camera rather than on the edge (Figs. S3 and S4 of Supplement 1).

In a comparison between ROSE-HSI and conventional wide-field imaging in rolling shutter mode, we demonstrated that ROSE-HSI faithfully reconstructs the action potentials (APs) within the same region of interest (ROI). We extracted optical waveforms obtained using the two methods from spike-triggered average (STA) movies of APs recorded in a cultured rat hippocampal neuron expressing the genetically encoded voltage indicator (GEVI) HVI-AF594 and the cation channelrhodopsin CheRiff [16,17] [Figs. 1(C)–1(H)]. The results reveal that ROSE-HSI yields a more desirable AP shape under the same available field of view (FoV) [Fig. 1(C)]. Owing to a threefold increase in equivalent frame rate and the elimination of asynchronous exposure, ROSE-HSI achieved a narrow full width at half maximum (FWHM) (ROSE-HSI is $21.6 \pm 6.7\%$ narrower than imaging in rolling shutter mode) and a higher response sensitivity ($19.0 \pm 5.4\%$ higher in ROSE-HSI) than wide-filed imaging in rolling shutter mode, as expected [Figs. 1(D)–1(E), Fig. S5A of Supplement 1].

On the other hand, when comparing 1 kHz ROSE-HSI with 1 kHz imaging in rolling shutter mode (with only one-third of the FoV of ROSE-HSI) [Fig. 1(F)], ROSE-HSI does not compromise the acquired AP waveforms in FWHM [$1.4 \pm 9.7\%$ longer in ROSE-HSI, Fig. 1(g)]. Despite a statistically significant difference, the response sensitivity exhibits only a modest change in response magnitude [$8.0 \pm 2.9\%$ lower in ROSE-HSI, Fig. 1(H), and Fig. S5B of Supplement 1], confirming the robustness of extending 1 kHz imaging to a threefold larger square FoV in ROSE-HSI. The modest sensitivity loss in reporting AP spikes is unlikely due to GEVI impairment under the stroboscopic illumination used in ROSE-HSI [13]. Instead, it is probably caused by the image processing steps, namely, brightness correction, six-channel registration, and background subtraction.

ROSE-HSI demonstrates clear advantages in mapping AP propagation along dendrites from voltage imaging data, which require movies with high temporal resolution and accuracy (Fig. S6 of Supplement 1). AP spike trains were evoked in two FoVs, each containing a neuron co-expressing the voltage indicator Solaris585 [18] and the optogenetic actuator CheRiff-EGFP (Fig. S6A–B). We then generated and compared AP arrival timing maps for these neurons. The maps were derived from spike movies acquired with 1 kHz ROSE-HSI and 333 Hz rolling shutter imaging, with both movies upsampled to 1000 kHz via sub-frame interpolation. To mitigate rolling shutter-induced vertical delay, some studies [19–21] added a row-specific correction time (4.868×10^{-3} ms per row from the top of the FoV) after interpolation (Fig. S1A and Fig. S6C of Supplement 1). However, our results indicated that this correction did not effectively eliminate the exposure delay artifact in 333 Hz imaging. In contrast, 1 kHz ROSE-HSI in the same FoV produced more reliable timing maps (Figs. S6D–E; Fig. S6D and E of Supplement 1 correspond to the neurons in Figs. S6A and B of Supplement 1, respectively). APs appeared first around the soma and then propagated radially along neurites at speeds between 100 and 400 μm/ms (left panel in Figs. S6D–E of Supplement 1, highlighted in yellow).

Conversely, the raw 333 Hz rolling shutter imaging data (right panel in Figs. S6D–E of Supplement 1, highlighted in gray and outlined with a black dashed line) displayed an AP arrival time trend progressing from the bottom to the top of the FoV, independent of neuronal polarity. Even after applying the delay correction, the propagation patterns remained abnormal (right panel in Figs. S6D–E of Supplement 1, highlighted in gray and outlined with a red dashed line). The corrected map showed AP arrival beginning at the top and progressing downward, suggesting overcorrection (right panel of Figs. S6D of Supplement 1). In another case, although APs initially appeared around the soma, a delay of over 3 ms to the distal neurites resulted in an abnormally slow propagation speed (well below 100 μm/ms) and a reduced speed along neurites parallel to the horizontal axis (right panel of Fig. S6E of Supplement 1). These findings indicate that despite partial correction of rolling shutter artifacts, ROSE-HSI provides superior temporal resolution for mapping fast events such as AP propagation at pixel resolution.

Compared to conventional 1 kHz rolling shutter imaging, ROSE-HSI also enhances the temporal accuracy of resolving AP waveforms by eliminating rolling shutter-related artifacts (Fig. S7 of Supplement 1). For instance, when extracting AP waveforms from three adjacent regions (top, middle, and bottom of the soma, corresponding to regions 1, 2, and 3 in Fig. S7A of Supplement 1) in a neuron co-expressing HVI-AF594 and CheRiff-EGFP [Fig. S7A of Supplement 1, the same neuron shown in Fig. 1(F)], 1 kHz ROSE-HSI produced consistent averaged traces with a similar width, depolarization speed, and repolarization speed (Figs. S7B–C of Supplement 1). These results align with synchronized AP bursts observed with a high-density microelectrode array (HD-MEA) [22]. In contrast, the same regions imaged with the 1 kHz rolling shutter mode yielded traces with reversed temporal order (from the bottom to the top of the soma) relative to the exposure sequence (Fig. S7B of Supplement 1), indicating interference from the rolling shutter and a loss of temporal accuracy. This artifact could not be totally eliminated by using the exposure delay correction to the traces of rolling shutter mode on the time series of each pixel in each ROI after interpolation to 102 kHz, with much larger differences remaining in the rolling shutter mode between the traces of region 2 or region 3 compared to region 1 regarding the time to first reach 30%–90% of maximum fluorescence change (Fig. S7C of Supplement 1). Overall, these data demonstrate that even at 1 kHz, ROSE-HSI outperformed conventional rolling shutter imaging in both waveform resolution and FoV size.

We next measured the FoV of ROSE-HSI at an optical linear magnification of 12.8, confirming that the galvo mirror does not introduce image distortions [Fig. 2(A)]. A 50 μm grid was imaged using conventional wide-field imaging in rolling shutter mode and ROSE-HSI at a sampling rate of 1 kHz. ROSE-HSI produced 3.6 times more horizontal lines than the conventional method [Fig. 2(A)]. Notably, due to optical component constraints, the maximum number of vertical lines in ROSE-HSI is 700, which is approximately one-third of the camera target. In traditional rolling shutter imaging, the maximum number of horizontal lines is 204, yielding a maximum square FoV flux of 83.2 Mpixels/s on two cameras (2×1000 Hz $\times 204 \times 204$ pixels). By sequentially projecting the fluorescent signal into six positions on two sCMOS cameras under global exposure mode at 166.6 Hz, ROSE-HSI attains a sixfold increase in pixel throughput relative to traditional rolling shutter imaging, eliminating temporal bias and achieving a maximum flux of 512.4 Mpixels/s (1000 Hz $\times 700 \times 732$ pixels). For comparison, 1 kHz rolling shutter imaging achieves a maximum flux of 470.0 Mpixels/s in a rectangular FoV (2304×204 pixels), which is 9.0% lower than that of ROSE-HSI.

Importantly, the near-square FoV of ROSE-HSI is more suitable for fast biological imaging than the rectangular FoV produced by rolling shutter methods, as it better captures two-dimensional propagation events (e.g., electrical activity across multiple neurites or calcium/voltage waves in cardiomyocyte populations) and minimizes out-of-FoV illumination, thereby increasing the photon budget and reducing photobleaching and phototoxicity. Even when considering the horizontal lines of the two cameras are spliced, the maximum number of imaging lines can only reach 408 at 1 kHz, and the corresponding maximum square imaging flux on the two cameras is 166.4 Mpixels/s (1000 Hz $\times 408 \times 408$ pixels), which is only 32.5% of ROSE-HSI. Under a total magnification time of 12.8, ROSE-HSI can reach a maximum FoV of 350×366 μm.

We further verified the temporal resolution of ROSE-HSI by monitoring fluorescence signals excited by a constant laser controlled by a two-dimensional galvo mirror [Fig. 2(B)]. The laser excitation region was programmed to move in a circular path with periods of 10, 6, and 3 ms. With 1 kHz ROSE-HSI, fluorescence

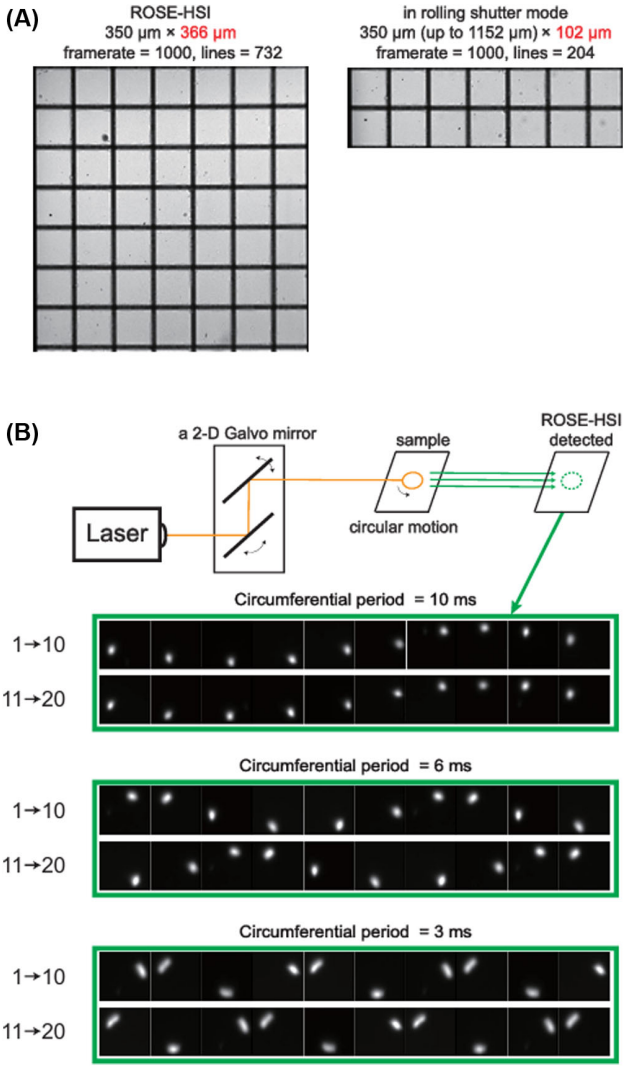

Fig. 2. FoV and time resolution verification of ROSE-HSI. (A) FoV test of ROSE-HSI. 50 μm grid (Thorlabs, R1L1S1P) was imaged with traditional wide-field imaging in rolling shutter mode and ROSE-HSI at a sampling rate of 1 kHz, respectively. ROSE-HSI has a clear advantage in the number of verticle lines. (B) Time resolution verification of ROSE-HSI. A two-dimensional galvo mirror controlled a constant laser to excite the fluorescence signals, and the laser was circularly moved with different periods of 10, 6, and 3 ms, respectively. The subframes recorded by 1 kHz ROSE-HSI exhibit that the fluorescence signals appeared at fixed positions in each phase of the laser modulated with different motion frequencies, which proves that the temporal resolution of ROSE-HSI is 1 ms.

trajectories remained fixed in position on the FoV, with no phase shift relative to the laser motion, even at frequencies up to 333 Hz, confirming that ROSE-HSI achieves a temporal resolution of 1 ms [Fig. 2(B)]. These features enable ROSE-HSI to deliver a 1 kHz frame rate over a larger, near-square FoV, making it highly suitable for biological imaging applications, such as recording AP spikes across large neuronal populations.

3. RESULTS

Expanding the FoV enabled us to showcase the capability of 1 kHz ROSE-HSI in simultaneously resolving APs on adjacent neurons. By optogenetically stimulating neurons expressing CheRiff and HVI-AF594, ROSE-HSI faithfully captured the details of single-trial APs on the soma of multiple neurons, along with the corresponding back-propagating APs (bpAPs) on various neurites (Fig. 3). During extended optogenetic stimulation, ROSE-HSI exhibited the ability to record high-frequency AP bursts with intervals as narrow as 10 ms (Fig. S8 of Supplement 1). By capturing events in their natural sequence through single-time acquisition, ROSE-HSI facilitates high-fidelity voltage imaging for spontaneous AP firing at a 1 kHz frame rate. We performed four rounds of 5 min imaging on a neuron expressing HVI-COT-Cy3 [23], monitoring changes in burst frequency of spontaneous APs under treatment with drugs targeting various synaptic receptors (Fig. S9 of Supplement 1). Furthermore, we demonstrated ROSE-HSI's capability in recording synaptic neurotransmitter-mediated AP bursts in multiple neurons induced by local uncaging of MNI-caged-L-glutamate [24]. ROSE-HSI could distinguish the AP bursts within intervals as short as 27 ms while maintaining adequate SNR in a 2 min consecutive recording (Fig. S10 of Supplement 1).

We subsequently applied ROSE-HSI to investigate the initiation and propagation of AP in neuronal populations. To visualize the axon initial segment (AIS), a 10–50 μm length region on the proximal axon where action potentials (APs) originate, we performed live-cell immunostaining of the AIS marker protein, neurofascin 186 (NF186) [25,26] [Fig. 4(a)]. In a rat hippocampal neuron expressing the voltage indicator HVI-Cy5, 1 kHz ROSE-HSI illustrated the initiation and propagation of APs across the neuron within a 350 × 300 μm FoV. By interpolating the STA movie generated from 64 evoked AP signals [17,27], we clearly observed AP initiation at the AIS, followed by its backward propagation to the soma and subsequently to the surrounding dendrites [Figs. 4(B) and 4(C)]. ROSE-HSI also enabled simultaneous reports of AP firing dynamics in four adjacent neurons under global optogenetic stimulation within a 1.8 ms duration [Figs. 4(D)–4(F)]. Utilizing sub-frame interpolation, ROSE-HSI visualized AP propagation from the soma to the distal neurites within a single neuron. Concurrently, it captured the onset of depolarization and AP firing at the soma of an adjacent neuron [Fig. 4(F), for more details please see Visualization 1]. Asynchronous AP initiation among the four neurons may be attributed to varying intrinsic excitability and/or expression levels of the actuator CheRiff. These data suggest that compared to the conventional methods that imaging in rolling shutter mode, ROSE-HSI can effectively map the AP spiking sequence and inter/intracellular propagation within the millisecond–micrometer scale with superior information flux in a larger FoV. Furthermore, ROSE-HSI successfully mapped the AP propagation across two neurons even when the number of spikes for the averaging movie was as few as two, attributed to the robust SNR of kilohertz AP imaging maintained in the ROSE-HSI technique (Fig. S11 of Supplement 1).

We went on to monitor the details of bidirectional propagation of AP from the AIS to other compartments. The speed of AP propagation, both forwardly toward the distal axon and backwardly toward the soma and dendrite, is a pivotal parameter modulating spike-timing-dependent plasticity (STDP) in neuron populations, which significantly influences synaptic transmission and the establishment of synaptic plasticity, such as long-term potentiation (LTP) [28–31]. The propagation of AP to axon and dendrite culminates in local depolarization at either presynaptic or postsynaptic sites, and the speed of the propagation defines the

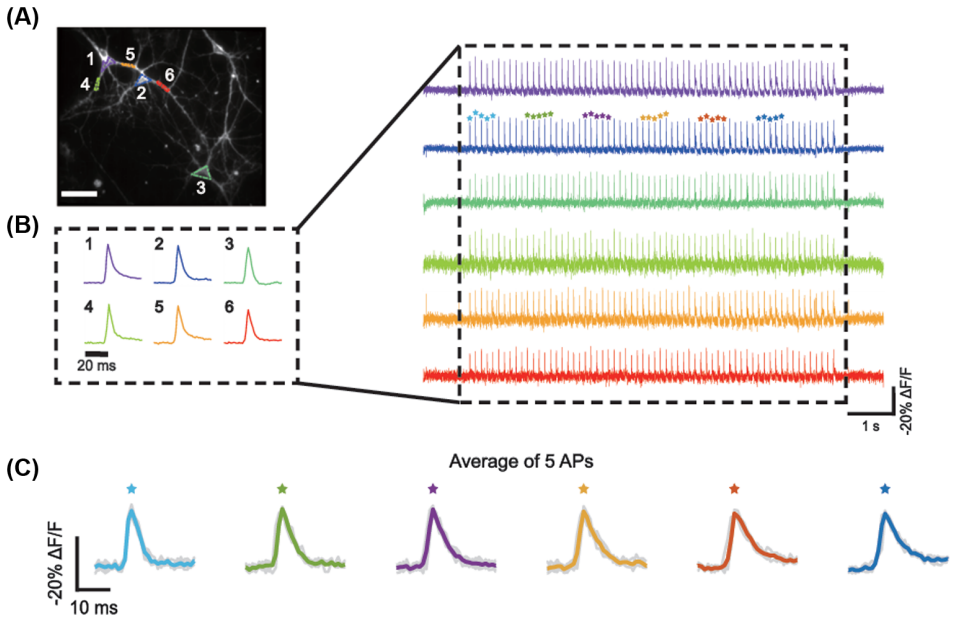

Fig. 3. Simultaneous AP imaging in multiple neurons by 1 kHz ROSE-HSI. (A) Multiple neurons co-expressing HVI-AF594 and CheRiff-EGFP. Six ROIs belonging to three neurons are circled in different colors. Data were acquired with a magnification time of 12.8, scale bar = 50 μm. (B) AP trains evoked by global optogenetic stimulation extracted from corresponding regions in (A). The averaged traces of 64 APs are highlighted in the dashed line box on the left. (C) AP signals averaged from five consecutive single-trial APs from region 2 of (A) and (B). The single-trial APs used for taking averages are marked with asterisks in (B) in corresponding colors.

brief millisecond-scale windows built up by the accurate chronological sequence of AP arrivals at pre- and post-synaptic regions [32–34]. The speed of bidirectional AP propagation on retinal neurons, hippocampal dentate granule cells, hippocampal CA1, and Layer 5 cortical pyramidal neurons have been measured via electrical and optical methods, proving that propagation velocity and its decay are related to the types and morphologies of neuron and neurites [21,35–39]. However, the spatial resolution and acquisition intervals of these measurements have been limited in their capacity to resolve velocities over short neurite distances or to conduct simultaneous measurements across multiple regions [22]. To achieve this, we calculated the speed of backpropagating AP on the AIS to soma and found that speed distinguishment when APs were evoked via various approaches. We performed localized optogenetic stimulation on soma, AIS, and dendrite (with a similar distance from the soma as the AIS and equal illumination dose) for AP spiking trains, using a 20–mm diameter spot controlled by a 2D galvo mirror on the neurons co-expressing CheRiff and Solaris$_{585}$ [18] [Fig. 5(A)]. We subsequently quantified the propagation velocity in the region between AIS and the soma from the extracted voltage imaging data on them, a measurement challenging to achieve via conventional electrical methods [Fig. 5(B)]. We observed the propagation speed of AP along the AIS to the soma at a range from 60 to 368 μm/ms, with a significant reduction when AP was directly activated by optogenetic stimulation at the AIS (157.3 ± 32.6 μm/ms), as compared to APs activated by stimulation of the soma (228.6 ± 35.2 μm/ms) or dendrites (200.2 ± 47.4 μm/ms) [Fig. 5(C)]. On the contrary, we found that when using the same light dose to stimulate both the AIS and dendrites in proximity to the soma, the delay in AP firing (relative to the start of the blue light, i.e., AP latency) was significantly shorter in cells when stimulated at the AIS (10.2 ± 1.0 ms) than at proximal dendrite (13.2 ± 1.4 ms) [Fig. 5(D)].

We subsequently visualized the variety of AP properties at the different sites on the axon. AP propagation along the axon from the AIS toward its distal end conveys information encoded by the diversity of frequency, shape, and interval of AP [40]. Alterations in AP on propagation speed and waveform shapes have been reported at various sites along the axon, influenced by the local morphology and level of ion channel expression on the axon [12,41–43]. Due to the expanded FoV provided by ROSE-HSI, we were able to monitor the AP waveform on both the proximal axon adjacent to the soma and the distal axon extending beyond 200 μm from the soma, facilitating the measurement of bidirectional AP propagation along the axon. In this selected FoV, we resolved the AP arrival timing at the sites on the axon [Figs. 5(E)–5(G)]. As expected, the AP is initiated at the AIS and bidirectionally propagates toward the soma and distal axon [Fig. 5(F)]. Our findings reveal that forward propagation to the distal axon is faster than backward propagation on the AIS, regardless of whether localized stimulation was conducted on the AIS (forward to distal axon: 393 μm/ms; backward to soma: −61 μm/ms) or soma (forward to distal axon: 315 μm/ms; backward to AIS: −199 μm/ms) [Fig. 5(F)]. On the other hand, the FWHM of the AP waveform from the soma, proximal neurites (including dendrites and AIS that were 50 μm from the soma), and distal axon (150 μm from the soma) exhibits that the AP propagating to the distal axon (3.44 ± 0.32 ms) has shorter FWHM than that of AIS (4.48 ± 0.40 ms), proximal dendrite (4.26 ± 0.41 ms), or soma (4.28 ± 0.39 ms), aligning with previous data analyzed from voltage imaging data with multiple acquisitions [12,27] [Figs. 5(G) and 5(H)]. These data demonstrate that ROSE-HSI enables studying the velocity and waveform heterogeneity of action potentials during bidirectional transmission along axons, offering a significantly higher throughput compared to conventional methods that image in rolling shutter mode in a single acquisition.

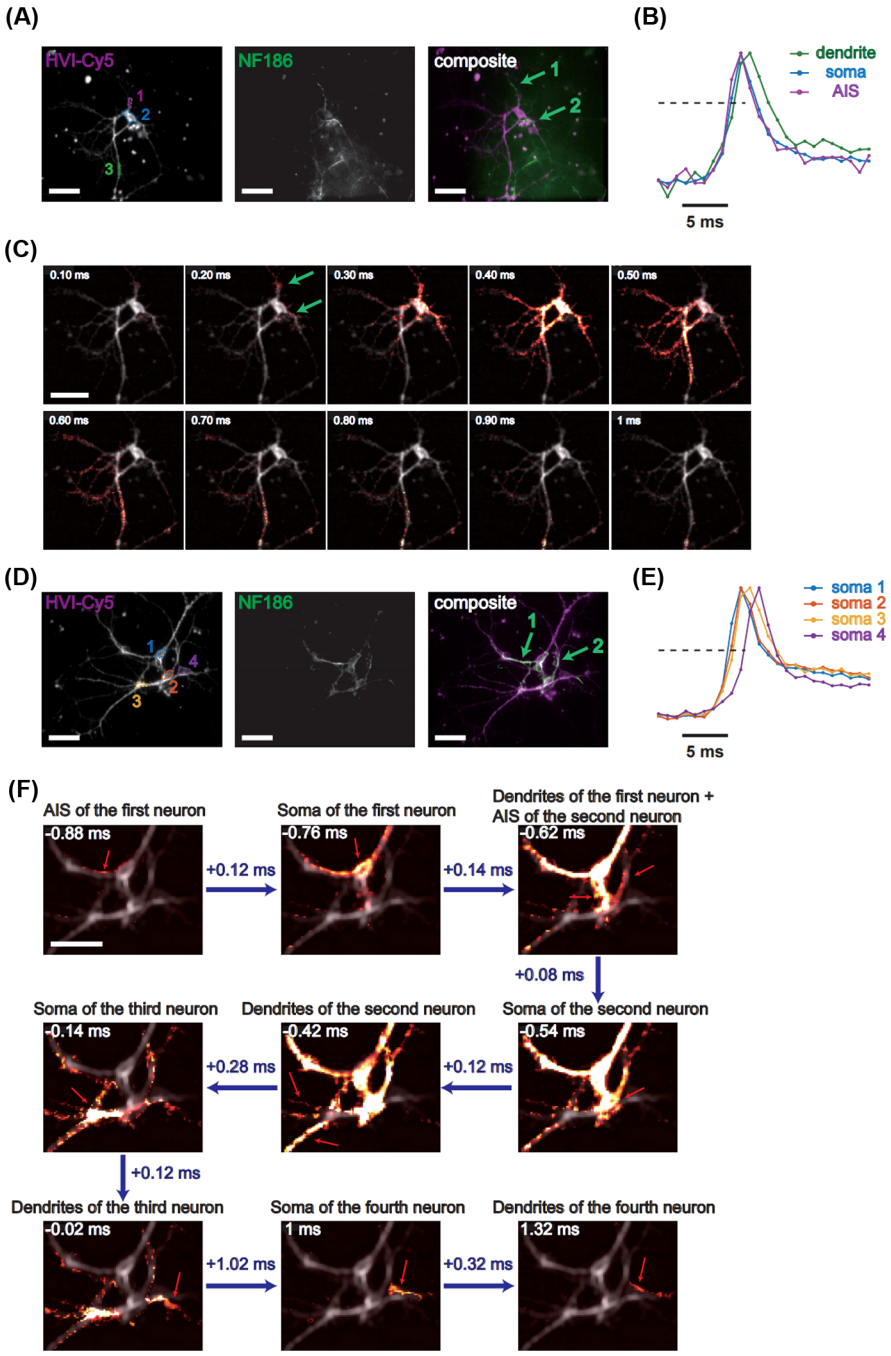

Fig. 4. Mapping AP initiation and propagation with 1 kHz ROSE-HSI. (A) Left: ROSE-HSI image of the rat hippocampal neuron co-expressing HVI-Cy5 (639 nm: 20 W/cm^2) and CheRiff-EGFP. Center: the AIS of the neuron indicated by living-cell immunostaining of NF186. Right: overlaid image. The green arrows point out the AIS (NF186), where arrow 1 is more like the AIS of the target neuron. Data were acquired with a magnification time of 12.8, scale bar = 50 μm. (B) The AP waveforms extracted from the selected ROIs of AIS (in purple), soma (in blue), and dendrite (in green). Traces are normalized using min-max scaling. The dashed line represents 60% of the maximum fluorescence change, which serves as the threshold used to determine the timing of AP arrival during the propagation. (C) The keyframes of AP initiation and propagation from the spike-triggered averaged movie from 64 APs after pixel-by-pixel linear interpolation. The relative AP arrival timing on each pixel is defined as the first time that the change of fluorescence exceeds the threshold. The calculated timing in the FoV is normalized by centering, with zero representing the mean of the arrival times in every pixel. (D) ROSE-HSI images of four neighboring rat hippocampus neurons and their labeled AIS. (E) The AP waveforms extracted from the soma of the four neurons (in blue, orange, yellow, and purple). The traces are normalized using min-max scaling. The dashed line represents 60% of the maximum fluorescence change like (B). (F) The selected keyframes of the averaged movie of the sequential firing of AP in four adjacent neurons after pixel-by-pixel linear interpolation. APs were triggered by global optogenetic stimulation (64 times for the average movie). The relative AP arrival timing on each pixel is defined as the first time that the fluorescence exceeds the threshold. The calculated timing in the FoV is normalized by centering, with zero representing the mean of the arrival times in every pixel. Red arrows in the images point to the sites where the AP has just arrived within each neuron. Blue arrows indicate chronological order.

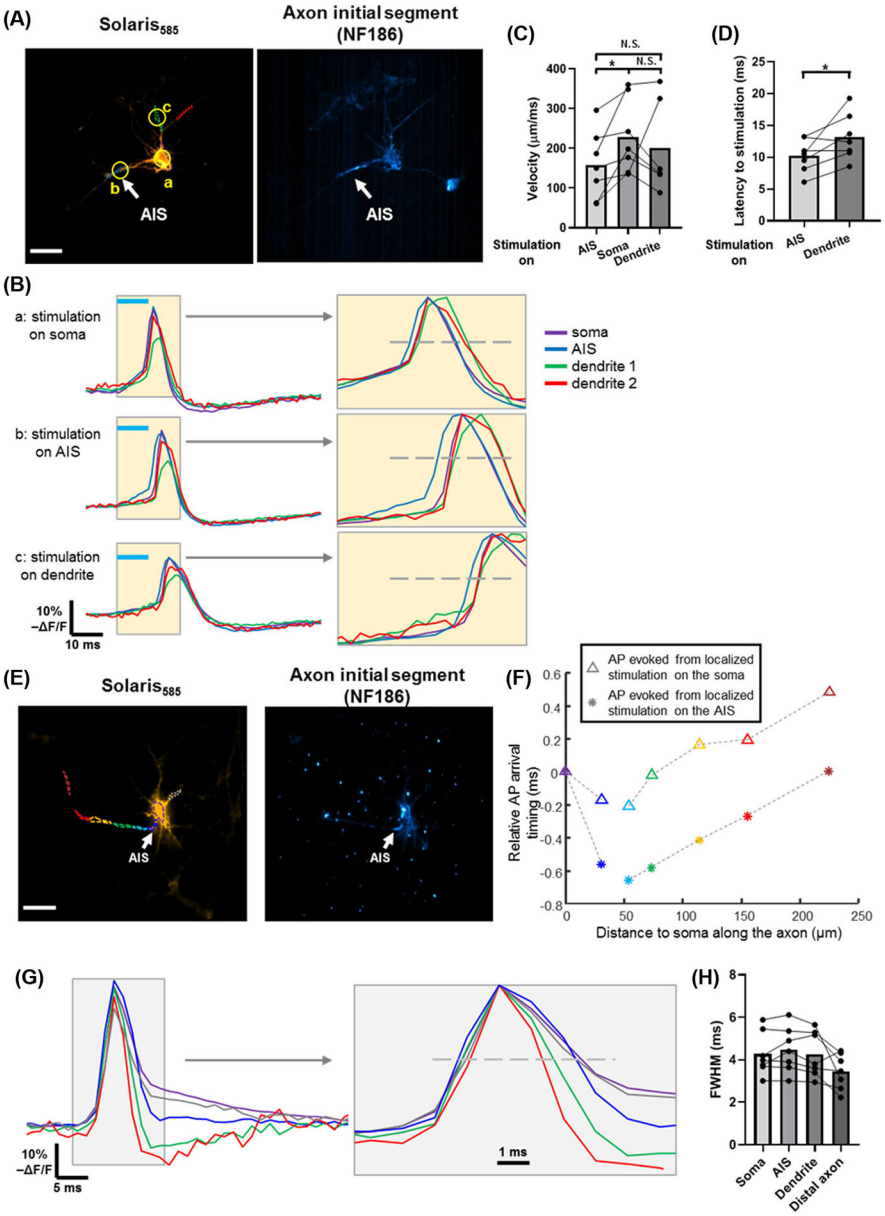

Fig. 5. 1 kHz ROSE-HSI records the bidirectional propagation of action potentials in cultured neurons. (A) Fluorescent images of a cultured hippocampal neuron co-expressing Solaris$_{585}$ and CheRiff (left) and live cell immunostaining of NF186 (right), which reveals the location of AIS and the extending axon. Three yellow circles on the left image indicate the regions of localized optogenetic stimulation on the soma (a), AIS (b), and a proximal dendrite on the neuron. Four ROIs, outlined by the dashed lines, represent the soma (violet), AIS (cyan), and two proximal dendritic regions (green and red) of the neuron for extracting voltage imaging data. (B) The averaged action potential traces extracted from the four ROIs evoked by the localized optogenetic stimulation on the three round regions in (A). The blue lines represent the positions (10 ms duration) of optogenetic stimulation. The zoom-in displays on the right encompass a time range (20 ms) surrounding the rising edge and peak position of each AP (highlighted in yellow; each trace is normalized to a 0–1 range). The gray dashed lines indicate the 60% position of the maximum fluorescence change of AP as the threshold for calculating AP's arrival timing at each site. (C) The speed of backpropagating action potential from AIS to the soma, when the AP was evoked from localized optogenetic stimulation on AIS, soma, or the proximal dendrite region at a similar distance to the soma to the AIS on each cell (N = 7). (D) The AP latency recorded at the soma of neurons (N = 7) during 10 ms localized optogenetic stimulation with the same illumination dose on AIS or a proximal dendrite region at a distance from the soma equivalent to that of the AIS. (E) Fluorescent images of a cultured hippocampal neuron co-expressing Solaris$_{585}$ and CheRiff (left) and live-cell immunostaining of NF186 (right). Eight ROIs, outlined by the dashed lines, represent the soma (violet), AIS (blue), and a proximal dendritic region (gray), and five regions along the axon (cyan, green, orange, red, and brown) of the neuron for extracting voltage imaging data. (F) The relative action potential (AP) arrival timing (normalized to $t_{soma} = 0$) on the axon calculated from the neuron depicted in (E). The timing data are represented by asterisks and triangles in various colors corresponding to the outline of the somatic and axonal ROIs in (E). The asterisks and triangles represent the timing of AP spike trains evoked by localized stimulation on the AIS and soma, respectively. (G) The averaged action potential traces extracted from the five ROIs evoked by the 10 ms localized optogenetic stimulation on the AIS in (E). The zoom-in displays on the right encompass a time range (10 ms) surrounding the spiking peak of each trace (highlighted in gray; each trace is normalized to a 0–1 range). The gray dashed line indicates the 50% position of the maximum fluorescence change of AP for calculating the FWHM of each trace. (H) The FWHM of AP (evoked by optogenetic stimulation on the soma) recorded on the soma, AIS, proximal dendrite (50 μm to the soma), and distal axon (150 μm to the soma) (N = 7). In the calculation, the AP waveforms were averaged from the traces of 20–50 APs evoked by the 4 Hz, 10 ms optogenetic stimulation. Data were acquired with a magnification time of 14.4, scale bar = 50 μm.

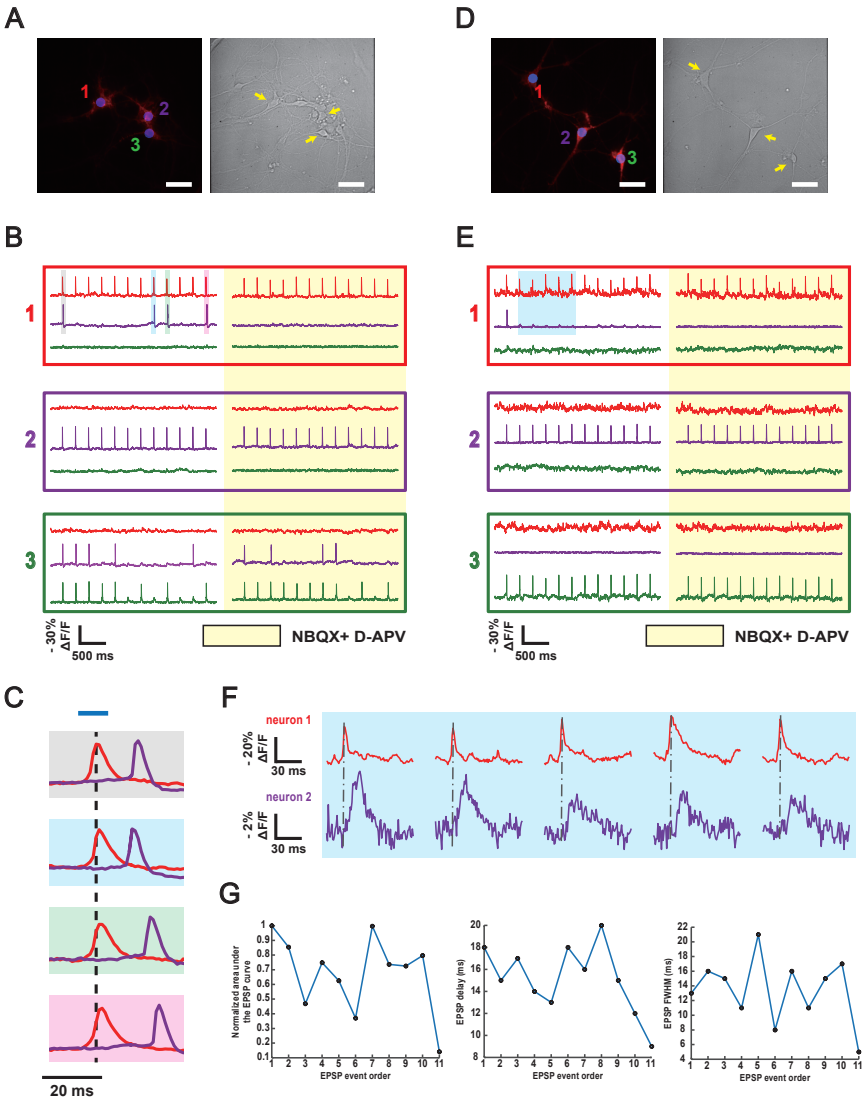

Fig. 6. Interrogating the action potential firing mediated by synaptic connections in cultured neuron populations using ROSE-HSI. (A) Fluorescent and brightfield images of neuron populations expressing Solaris$_{585}$ and CheRiff. The neuron numbers represent the orders of local stimulation, with the blue circle denoting the range of corresponding stimulation. Scale bar = 50 μm. (B) Representative responses of selected neurons 4 Hz 10 ms single-cell stimulation, recorded using 1 kHz ROSE-HSI before and after 5 min treatment of NBQX (10 μM) and D-APV (25 μM). The numbers correspond to the stimulation ranges in (A). (C) A zoom-in display of the synaptic-mediated paired AP signals in neurons 1 and 2 highlighted in (B). (D) Fluorescent and brightfield images of the other neuron populations expressing Solaris$_{585}$ and CheRiff like (A), scale bar = 50 μm. (E) Representative responses of selected neurons 4 Hz 10 ms single-cell stimulation, recorded using 1 kHz ROSE-HSI before and after 5 min treatment of NBQX (10 μM) and D-APV (25 μM). The numbers correspond to the stimulation ranges in (D). (F) A zoom-in display of the synaptic-mediated paired AP signals in neighboring neurons 1 and 2 highlighted in (E). (G) The trends in the normalized area under the V_m change curve (left), delay to the presynaptic AP (center), and FWHM (right) of the selected 11 EPSP events. Data were acquired with a magnification time of 14.4, scale bar = 50 μm.

We next implemented ROSE-HSI to interrogate synaptic transmission in cultured neuron populations expressing CheRiff and Solaris$_{585}$. Through localized optogenetic stimulation at single-neuron resolution, we measured pair-wise synaptic connections between the stimulated neuron and its neighbors. The high throughput of 1 kHz ROSE-HSI imaging allowed us to map the timing of AP firing in synaptically connected neurons within 20 ms [Figs. 6(A)–6(C)]. The paired AP firings were eliminated after treatment with the ionotropic glutamate receptor antagonists NBQX (10 μM) and D-APV (25 μM) [Fig. 6(B)]. In the postsynaptic neuron, four APs exhibited short intervals of 14, 11, 16, and 19 ms relative to the presynaptic AP elicited by blue-light stimulation [Fig. 6(C)]. The identification of AP delay differences in synapse-connected neurons via ROSE-HSI suggests that this approach enables the monitoring of dynamic changes in synaptic strength and the viability of key synaptic transmission-related proteins, such as ionotropic α-amino-3-hydroxy-5-methyl-4-isoxazolepropionic acid (AMPA) receptors, with millisecond-level kinetics [44,45]. The subthreshold excitatory postsynaptic potentials (EPSPs) were also captured with an SNR of 7.6 ± 1.0 and were abolished by treatment of NBQX and D-APV [Figs. 6(D) and 6(E)]. The variation in the indexes of time integral, latency to the evoked AP, and duration (FWHM) of recorded single-trial EPSPs were also well-determined from the recording [Figs. 6(F) and 6(G)]. From these parameters of the spiking/subthreshold responses from the neurons around the locally stimulated one

reported by ROSE-HSI, the synaptic connectome could be thoroughly profiled at the micrometer-millisecond scale [46,47].

4. DISCUSSION

Voltage imaging captures millisecond-scale membrane potential fluctuations in individual neurons or neural populations. Although it provides richer information than other functional imaging modalities, its much faster frame rate imposes stricter technical demands [1,2]. Despite continuous improvement in voltage indicators over the past decade, the overall acquisition rate and throughput of voltage imaging remain constrained by slow advancements in detector technology [1]. While sCMOS cameras offer superior spatial resolution, throughput, and noise performance compared to EMCCD cameras at equivalent frame rates [8,48], they still face limitations in acquisition rate and timing accuracy, even in their fastest rolling shutter mode.

In this work, we introduce ROSE-HSI, a method that overcomes the vertical throughput limitations and timing inaccuracies caused by exposure delays in the sCMOS camera used for voltage imaging. By integrating two-camera recording with galvo mirror-based parallel projection, which has been previously applied to enhance throughput in large-scale functional imaging [10,49–51], ROSE-HSI produces a near-square FoV that extends vertically to more than three times the size achieved with conventional rolling shutter imaging. This expanded near-square FoV not only optimizes two-dimensional acquisition in a single frame, thereby improving monitoring of radial ROIs such as multiple neurites from one neuron or the propagation of calcium and membrane potential waves in cultured cardiomyocytes, but also improves the photon budget by preferentially exciting the target area, which minimizes out-of-FoV illumination and reduces both photobleaching and phototoxicity. These benefits are crucial for live-cell imaging.

ROSE-HSI also addresses the asynchronous exposure and readout issues inherent in rolling shutter operation. Ideally, a "global shutter", where all images are exposed simultaneously, is best for fast imaging. However, standard sCMOS cameras only support "global exposure", meaning that while the exposure start is identical across lines, the duration varies. To simulate a true global shutter, the ROSE-HSI system employs two sCMOS cameras and sequentially projects the fluorescent signal into six different positions during one exposure period. This strategy circumvents the asynchronous termination seen in global exposure. Although projecting more sub-images could further improve temporal accuracy and increase the acquisition rate, it would also reduce the laser excitation duty cycle and lower the pixel flux per sub-frame, thus potentially introducing additional noise and diminishing spatial detail.

From an optical design standpoint, the imaging path of ROSE-HSI uses separate lens groups for each sub-path after the one-dimensional galvo mirror to minimize aberrations. A more than four-way projection is not suitable for this lens group design due to insufficient space for proper adjustment (Fig. S2 of Supplement 1). Considering that 1 kHz voltage imaging (achieved by six sub-paths over two cameras) is generally sufficient to capture fast signals such as the AP waveform and meets the kinetic response needs of GEVIs, we opted to collect three sub-images per frame. It is worth noting that another study similarly used a galvo mirror-based fast projection of sub-images into a single exposure in rolling shutter mode, significantly enhancing acquisition rates in live-cell structured illumination microscopy [10].

There are simpler technologies that appear to make it easier to image at 1 kHz with a large FoV, but they also present potential problems. For example, using an ultra-high-speed sCMOS directly, or a knife-edge prism can be used to split the image and then project it onto two cameras for synchronous imaging. While some ultra-high-speed sCMOS cameras (e.g., HiCAM Fluo) offer higher flux levels, achieving 1 kHz (12 bit) or even 2 kHz (8 bit) imaging in full frame with electronic global shutter, their low quantum efficiency (Q.E.) and imaging depth are unacceptable for voltage imaging, where the sensitivity and brightness of GEVIs are limited [1]. The second method may cause asynchronous sampling of different rows due to the rolling shutter. If global exposure is used, there will be a "dead time" when the dual cameras are reading at the same time, which limits the actual number of imaging lines.

Unlike methods that enhance voltage imaging data by using repetitive, multiple-round stimulation [12,13], ROSE-HSI can capture spontaneous events. This capability greatly improves its utility for studying neuronal activities with advanced genetically encoded indicators that deliver superior SNR. Moreover, ROSE-HSI is a highly integrated and adaptable voltage imaging module that can be readily combined with other imaging technologies, such as multiplexed imaging with Ca^{2+} or neural transmitter indicators [5,18,52]. Notably, since its modulation is confined to the fluorescence pathway and laser illumination, ROSE-HSI is compatible with upright microscopes and can be used for *in vivo* imaging in acute brain slices or live animals, highlighting its significant potential for further development.

5. METHODS

A. Optical Setup

The detailed optical setup can be found in Fig. S2 of Supplement 1. The entire optical system was built on the basis of the Olympus IX71 inverted microscope. A 639 nm 1 W single longitude laser (Laser 1, OPS-1033, Coherent), a 593 nm 150 mW laser (Laser 2, MLL-FN-594-100 mW, CNI), and a 532 nm 1 W laser (Laser 3, MGL-H-532-1 W, CNI) were modulated by an acoustic-optic modulator (AOM, CNI-AOM-T100, CNI) into 1 kHz pulsed lasers and then expanded by a beam expander (Beam Expander 1, GCO-2503, DHC). In the other direction, a 488 nm laser (Laser 4, WCP488-150FS-224, PIC) was coupled into the polarization-maintaining fiber. After being emitted from the fiber, the laser was collimated into a parallel beam by a fiber collimator. A dichroic mirror (DM 4) causes the four beams (Lasers 1–4) to merge into the same path. Then they were focused at the back focal plane of the objective [UPLXAPO 20X 0.8 NA dry objective (Olympus), or CFI75 Apo 25XC W 1.1 NA water dipping/immersion objective (Nikon, MRD77220)] by a lens to illuminate the sample from the bottom. Unlike these beams, a 405 nm laser (Laser 5, WCP405-150FS-224, PIC) was expanded by a beam expander (Beam Expander 2, GCO-2501, DHC) and passed through a two-dimensional galvanometer, and finally focused on the sample. The presence of a two-dimensional galvanometer allows the illumination area to be controlled (Fig. S10 of Supplement 1). Due to the needs of some experiments, Laser 4 and Laser 5 may be used interchangeably so that the illumination area of the 488 nm laser can be controlled in Figs. 5 and 6.

In the imaging path, the aperture first functioned as a field diaphragm to prevent the overlapping of sub-images on the camera. Then, the 1 kHz fluorescence signal was focused on a 166.667 Hz galvo mirror and reflected to form six fixed sub-channels. The reflected fluorescence signals were collimated by six pairs of conjugated lenses and projected onto two sCMOS chips (C14440-20UP, Hamamatsu), respectively. The scanning mirror was placed at the focus of six pairs of conjugate lenses, ensuring the image on the cameras was not blurred during the scanning process. When the fluorescence signal is scanned at the junction of two adjacent lenses, the laser must be turned off to prevent signal loss or crosstalk.

The AOM, sCMOS1, sCMOS2, and galvo mirror were synchronized by a National Instruments DAQ board with software written in LabVIEW (LabVIEW 2016, 16.0). The DAQ device first generated an internal reference clock. Then, the DAQ device generated control signals for the AOM, sCMOSs, and galvo mirrors based on the reference clock to achieve signal synchronization. The AOM was turned on periodically, allowing the laser to be modulated at a frequency of 1 kHz. The sCMOSs adopted the external-level global exposure trigger method, each camera included three AOM openings during one exposure process, so as to obtain three sub-images accordingly. The galvanometer scanned at a fixed frequency. The timing diagram is given in Fig. S3 of Supplement 1.

B. Channel (Sub-Image) Calibration

Image processing was performed by MATLAB software (MATLAB 2015b). First, the six-channel images were cut into similar areas of the same size as much as possible to reduce unnecessary visual field loss caused by subsequent calibrations. Then, the channel with the smallest fluorescence loss is used as a template for matrix transformation to completely match the positions of the six-channel images. The matrix transformations involved in this work all use the "similarity" template of the "imregtform" function in MATLAB, that is, the "translation + rotation + scale transformation" of the image. In order to ensure the accuracy of calibration, it is recommended that the maximum number of iterations when generating the T-transformation matrix is set to more than 5000. After the inter-channel position, further calibration of the brightness was required. Since the fluorescence loss caused by optical hardware was almost fixed, theoretically, the brightness calibration could be completed by multiplying the channel with a larger loss by a coefficient. However, due to the existence of unavoidable aberrations, pixel-level brightness calibration is sometimes necessary for fine pixel-level signal analysis (such as action potential propagation mapping).

C. Interpolation Method and Calculation of Action Potential Arrival Time

To map the action potential propagation based on the spike-triggered average (STA) movie calculated from ROSE-HSI recorded AP spikes, a sub-frame interpolation was applied to the normalized AP trace on each pixel. The Gaussian spatial filter and principal components analysis (PCA)-based temporal filter were introduced to the fluorescence signal on each pixel for an SNR increase [17]. Then the linear interpolation will be performed on the pixel of interest thresholded with the standard deviation in the average movie, achieving 1000-time upsampling on the AP waveform. On each pixel, the arrival timing of AP propagation was defined as the time that the fluorescence trace first passes over the customized threshold (60% or 70% of the maximum fluorescence change in this work), and the final propagation heat maps were conducted with a zero-mean normalization. The propagation movie from the sub-frame linear interpolation results was generated by a Gaussian time distribution with a $\Delta t = 0.025$ ms and a global-average temporal resolution $\sigma = 0.025$ ms. The brightest time of each pixel was equal to the arrival timing calculated above. The keyframes in Fig. 4 were selected from the corresponding movies and displayed sequentially.

D. Cell Culture

To prepare the cultured rat hippocampus neuron samples, the 14 mm glass bottom dishes or 12 mm sterilized glass coverslips (both from Cellvis) were first coated with a poly-D-lysine (10 μg/mL, Sigma-Aldrich) solution at 37°C with 5% CO_2 overnight. The coverslips and dishes were then rinsed twice with ddH_2O and then incubated with laminin mouse protein (10 μg/mL, Gibco) solution at 37°C with 5% CO_2 overnight. Thereafter, they were washed twice with ddH_2O and air-dried at room temperature for the following seeding.

For the dissection of hippocampal neurons, the heads of neonatal rats were separated from the bodies with scissors, and the brains were removed from the skull and placed into a 35 mm dish containing a pre-cooled dissection medium (high glucose DMEM supplemented with penicillin/streptomycin antibiotics). The hippocampi were isolated from the brain under a dissection scope, cut into small pieces (approximately 0.1 mm^3), and digested with 2 mL Trypsin–EDTA (0.25%, Gibco) at 37°C with 5% CO_2 for 15 min. The supernatant was gently removed and replaced with 1 mL DMEM containing 10% fetal bovine serum (FBS, Gibco, 10099141C). The tissue fragments were triturated via repeated pipetting for 1 min and incubated in an ice bath for 5 min. For the preparation of lipid-mediated transfection, the supernatant was diluted in neuron culture medium (Neurobasal Medium, 2% B-27 Supplement, 1% GlutaMAX Supplement, and 1% penicillin/streptomycin, all from Gibco) to a final cell density of 6.6×10^4 cells/mL. A total of 1 mL cell of suspension was added to each dish or each coverslip placed in the wells of the 24-well plate, and the medium was half-replaced with fresh medium once every 4 days. For the preparation of electroporation, one million cells were collected after gently centrifuging at 4°C for 5 min at 0.1 g for the subsequent electroporation.

E. Transfection

For lipid-mediated transfection, neurons were transfected on the 8th day *in vitro* (DIV8) via Lipofectamine 3000 Reagent (Invitrogen). For 12 mm coverslips placed in wells of a 24-well plate, 1000–1200 ng total plasmid DNA and 2–2.4 μL of Lipofectamine 3000 Reagent were separately diluted in Neurobasal Medium. Subsequently, the DNA solution was mixed with Lipofectamine 3000 Reagent and incubated with neurons for 40 to 60 min. Following this, the transfection reagent was replaced with a medium consisting of equal volumes of the original medium and fresh neuron culture medium. Transfected neurons are typically imaged at DIV10-15.

For electroporation performed on a Lonza 4D-Nucleofector, the collected one million cells were resuspended in a mixture of

electroporation buffer (P3 Primary Cell 4D X Kit L, V4XP-3024, Lonza; 100 μL per cuvette), combined with 5 μg of plasmids, transferred to the conductive polymer cuvettes, and then subjected to electroporation using the preset "Neuron, rat, brain Hi/Cx HE (high efficiency)" protocol. After electroporation, the solution was diluted by 500 μL RPMI-1640 (Life Technologies, 22400097) and incubated at 37°C with 5% CO_2 for 10 min. The neurons were then diluted to a final cell density of 2.5×10^5 cells/imaging dish (D35-14-1-N, Cellvis) using the neuron culture medium consisting of Neurobasal Medium, B-27 Supplement, GlutaMAX Supplement, and penicillin/streptomycin, as described above. The entire cell suspension was totally seeded onto the glass region of each imaging dish. After incubation at 37°C with 5% CO_2 for 3–5 h, the medium was fully replaced with fresh neuron culture medium, and the medium was half-replaced with fresh medium once every 4 days until imaging at DIV 10–15.

F. HVI Labeling of Cultured Hippocampal Neurons

Cultured rat hippocampal neurons expressing HVI (Ace2 D81C mutant) were incubated with a mixture of 5 μM engineered bacterial lipoic acid ligase mutant (^{W37V}LplA), 100 μM rel-(1 R-4 E-pR)-cyclooct-4-ene-1-yl-N-pentanoic acid carbamate (4-TCO), 1 mM ATP (Amresco), and 1 mM magnesium acetate (Sigma-Aldrich) in Tyrode's salt solution (Macgene Technology) for 30 min at 37°C with 5% CO_2 for PRIME labeling. The neurons were then gently washed with Tyrode's solution three times and then labeled with 1.5 μM COT-Cy3-tetrazine (gift from Zhixing Chen Lab, Peking University) or 0.8 μM AF594-tetrazine (Click Chemistry Tools) to the rhodopsin through the IEDDA reaction in Tyrode's solution for 15 (COT-Cy3-tetrazine) or 10 min (AF594-tetrazine). Neurons were rinsed another three times in the dark before the voltage imaging experiment was performed at room temperature in commercial Tyrode's solution.

G. JaneliaFluor (JF) Dye Labeling of Cultured Hippocampal Neurons

Cultured rat hippocampal neurons expressing Solaris (Ace2 rhodopsin with a circularly permuted HaloTag (cpHaloTag) inserted into its first extracellular loop) were incubated in Neurobasal Medium with 100 nM JF585 dye for 15 min at 37°C with 5% CO_2. After that, neurons were gently rinsed three times with Neurobasal Medium and then transferred to Tyrode's buffer for subsequent imaging.

H. Living-Cell Immunolabeling of the Axon Initial Segment (AIS)

To identify the position of the AIS on cultured rat neurons, the anti-pan-neurofascin (extracellular) antibody (A12/18) (anti-NFASC, Cat# 75-172, NeuroMab, USA, diluted to a final concentration of 0.6 μg/mL) was conducted to the neurons at 37°C with 5% CO_2 for a minimum of 40 min, and performed in conjunction with the labeling of HVI or Solaris dyes. Subsequently, cells were washed three times in Neurobasal Medium and incubated with the secondary antibody (goat anti-mouse-Alexa Fluor 488 IgG(H + L), cat# A-11029, ThermoFisher or goat anti-mouse-Alexa Fluor 647 IgG(H + L), cat# A-21236, ThermoFisher, with 1:1000 dilution) at 37°C with 5% CO_2 for 15 min. After this, cells were washed three times with Tyrode's buffer or Neurobasal Medium and then transferred to fresh Tyrode's buffer for imaging.

I. Dichroic Mirrors and Filters

Different dichroic mirrors (DM) and filters are placed in different cubes in the microscope (Table S1 of Supplement 1), to receive fluorescence signals excited by different wavelengths.

Funding. National Natural Science Foundation of China (92254306, T2225020, 32241027 to W.J., 32170704, 32322050 to L.G., 32088101 to P.Z., 32027901 to Tao Xu); Ministry of Science and Technology of the People's Republic of China (2022YFA1304700 to P.Z.); National Key Research and Development Program of China (2021YFA1301500, 2022YFC3400602 to W.J., 2024YFA1307403 to Weixing Li); Instrument development project of CAS (GJJSTD20210001 to Tao Xu.); National Science and Technology Innovation 2030 Major Program (2022ZD0211905 to L.G.); The Chinese Academy of Sciences Project for Young Scientists in Basic Research (YSBR-104 to W.J.); National Science and Technology Innovation 2030 Major Program (2022ZD0211900 to L.G.); Beijing National Laboratory for Molecular Sciences (BNLMS-CXXM-202403 to P.Z.); Beijing Natural Science Foundation (Z240009 to W.J.); The XplorerPrize 2024 In Advanced Interdisciplinary Studies (XPLORER-2024-1045 to W.J.).

Acknowledgment. We thank Prof. Zhixing Chen from Peking University for his assistance with compound synthesis. We thank Dr. Shuzhang Liu for his assistance with sample preparation and helpful discussion. Author contributions: all authors planned the study. S.X. and L.P. drafted the manuscript. S.X. and L.G. designed and built the optical system. L.P. and P.Z. performed the sample preparation. S.X. and L.P. jointly completed the data analysis. W.J., L.G., and P.Z. participated in the manuscript revision. All authors have given final approval for the manuscript to be published and have agreed to be responsible for all aspects of the manuscript.

Disclosures. L.G. and W.J. have a patent related to this work. The patent number is ZL 2020 2 1687222.2. All other authors declare no competing interests.

Data availability. Data underlying the results presented in this paper are not publicly available at this time but may be obtained from the authors upon reasonable request.

Supplemental document. See Supplement 1 for supporting content.

REFERENCES

1. Y. Xu, P. Zou, and A. E. Cohen, "Voltage imaging with genetically encoded indicators," Curr. Opin. Chem. Biol. **39**, 1–10 (2017).
2. T. Knöpfel and C. Song, "Optical voltage imaging in neurons, moving from technology development to practical tool," Nat. Rev. Neurosci. **20**, 719–727 (2019).
3. Z. Liu, X. Lu, V. Villette, *et al.*, "Sustained deep-tissue voltage recording using a fast indicator evolved for two-photon microscopy," Cell **185**, 3408–3425.e3429 (2022).
4. M. Kannan, G. Vasan, S. Haziza, *et al.*, "Dual-polarity voltage imaging of the concurrent dynamics of multiple neuron types," Science **378**, eabm8797 (2022).
5. Y. Han, J. Yang, Y. Li, *et al.*, "Bright and sensitive red voltage indicators for imaging action potentials in brain slices and pancreatic islet," Sci. Adv. **9**, eadi4208 (2023).
6. S. W. Evans, D.-Q. Shi, M. Chavarha, *et al.*, "A positively tuned voltage indicator for extended electrical recordings in the brain," Nat. Methods **20**, 1104–1113 (2023).
7. H. Tian, H. C. Davis, J. D. Wong-Campos, *et al.*, "Video-based pooled screening yields improved far-red genetically encoded voltage indicators," Nat. Methods **20**, 1082–1094 (2023).
8. B. Mandracchia, X. Hua, C. Guo, *et al.*, "Fast and accurate sCMOS noise correction for fluorescence microscopy," Nat. Commun. **11**, 94 (2020).
9. L. Song, H.-W. Lu-Walther, R. Förster, *et al.*, "Fast structured illumination microscopy using rolling shutter cameras," Meas. Sci. Technol. **27**, 055401 (2016).
10. X. Xu, W. Wang, L. Qiao, *et al.*, "Ultra-high spatio-temporal resolution imaging with parallel acquisition-readout structured illumination microscopy (PAR-SIM)," Light Sci. Appl. **13**, 125 (2024).

11. L. Oth, P. Furgale, L. Kneip, *et al.*, "Rolling shutter camera calibration," in *Proc. IEEE Comput. Soc. Conf. Comput. Vis. Pattern Recognit.* (2013).
12. V. G. Sabater, M. Rigby, and J. Burrone, "Voltage-gated potassium channels ensure action potential shape fidelity in distal axons," J. Neurosci. **41**, 5372–5385 (2021).
13. L. Peng and P. Zou, "Supertemporal resolution imaging of membrane potential via stroboscopic microscopy," Chem. Biomed. Imaging **1**, 448–460 (2023).
14. L. Gu, Y. Li, S. Zhang, *et al.*, "Molecular resolution imaging by repetitive optical selective exposure," Nat. Methods **16**, 1114–1118 (2019).
15. L. Gu, Y. Li, S. Zhang, *et al.*, "Molecular-scale axial localization by repetitive optical selective exposure," Nat. Methods **18**, 369–373 (2021).
16. S. Liu, C. Lin, Y. Xu, *et al.*, "A far-red hybrid voltage indicator enabled by bioorthogonal engineering of rhodopsin on live neurons," Nat. Chem. **13**, 472–479 (2021).
17. D. R. Hochbaum, Y. Zhao, S. L. Farhi, *et al.*, "All-optical electrophysiology in mammalian neurons using engineered microbial rhodopsins," Nat. Methods **11**, 825–833 (2014).
18. J. Yang, S. Zhu, L. Yang, *et al.*, "Solaris, a panel of bright and sensitive hybrid voltage indicators for imaging membrane potential in cultured neurons," bioRxiv, (2024).
19. Y. A. Hao, S. Lee, R. H. Roth, *et al.*, "A fast and responsive voltage indicator with enhanced sensitivity for unitary synaptic events," Neuron **112**, 3680–3696.e8 (2024).
20. Z. Y. Chen, L. Peng, M. Zhao, *et al.*, "Differences in action potential propagation speed and axon initial segment plasticity between neurons from Sprague-Dawley rats and C57BL/6 mice," Zool. Res. **43**, 615 (2022).
21. W. Tian, L. Peng, M. Zhao, *et al.*, "Dendritic morphology affects the velocity and amplitude of back-propagating action potentials," Neurosci. Bull. **38**, 1330–1346 (2022).
22. V. Emmenegger, M. E. J. Obien, F. Franke, *et al.*, "Technologies to study action potential propagation with a focus on HD-MEAs," Front. Cell. Neurosci. **13**, 159 (2019).
23. S. Liu, J. Ling, P. Chen, *et al.*, "Orange/far-red hybrid voltage indicators with reduced phototoxicity enable reliable long-term imaging in neurons and cardiomyocytes," Proc. Natl. Acad. Sci. U.S.A. **120**, e2306950120 (2023).
24. M. Canepari, L. Nelson, G. Papageorgiou, *et al.*, "Photochemical and pharmacological evaluation of 7-nitroindolinyl-and 4-methoxy-7-nitroindolinyl-amino acids as novel, fast caged neurotransmitters," J. Neurosci. Methods **112**, 29–42 (2001).
25. M. S. Grubb and J. Burrone, "Activity-dependent relocation of the axon initial segment fine-tunes neuronal excitability," Nature **465**, 1070–1074 (2010).
26. W. Zhang, Y. Fu, L. Peng, *et al.*, "Immunoproximity biotinylation reveals the axon initial segment proteome," Nat. Commun. **14**, 8201 (2023).
27. M. A. Popovic, A. J. Foust, D. A. McCormick, *et al.*, "The spatio-temporal characteristics of action potential initiation in layer 5 pyramidal neurons, a voltage imaging study," Physiol. J. **589**, 4167–4187 (2011).
28. P. J. Sjöström and M. Häusser, "A cooperative switch determines the sign of synaptic plasticity in distal dendrites of neocortical pyramidal neurons," Neuron **51**, 227–238 (2006).
29. J. C. Magee and C. Grienberger, "Synaptic plasticity forms and functions," Annu. Rev. Neurosci. **43**, 95–117 (2020).
30. D. J. Bakkum, Z. C. Chao, and S. M. Potter, "Long-term activity-dependent plasticity of action potential propagation delay and amplitude in cortical networks," PLOS one **3**, e2088 (2008).
31. M. Fuenzalida, D. SevillaFernandez de, A. Couve, *et al.*, "Role of AMPA and NMDA receptors and back-propagating action potentials in spike timing–dependent plasticity," J. Neurophysiol. **103**, 47–54 (2010).
32. H. Markram, J. Lübke, M. Frotscher, *et al.*, "Regulation of synaptic efficacy by coincidence of postsynaptic APs and EPSP," Science **275**, 213–215 (1997).
33. G. J. Kress and S. Mennerick, "Action potential initiation and propagation: upstream influences on neurotransmission," Neurosci **158**, 211–222 (2009).
34. D. E. Feldman, "The spike-timing dependence of plasticity," Neuron **75**, 556–571 (2012).
35. T. Nevian, M. E. Larkum, A. Polsky, *et al.*, "Properties of basal dendrites of layer 5 pyramidal neurons, a direct patch-clamp recording study," Nat. Neurosci. **10**, 206–214 (2007).
36. R. Krueppel, S. Remy, and H. Beck, "Dendritic integration in hippocampal dentate granule cells," Neuron **71**, 512–528 (2011).
37. S. D. Antic, "Action potentials in basal and oblique dendrites of rat neocortical pyramidal neurons," Physiol. J. **550**, 35–50 (2003).
38. P. Park, D. Wong-Campos, D. G. Itkis, *et al.*, "Dendritic excitations govern back-propagation via a spike-rate accelerometer," bioRxiv, (2024).
39. E. Hartveit, M. L. Veruki, and B.-J. Zandt, "Dendritic morphology of an inhibitory retinal interneuron enables simultaneous local and global synaptic integration," J. Neurosci. **42**, 1630–1647 (2022).
40. D. Debanne, E. Campanac, A. Bialowas, *et al.*, "Axon physiology," Physiol. Rev. **91**, 555–602 (2011).
41. M. H. P. Kole, J. J. Letzkus, and G. J. Stuart, "Axon initial segment Kv1 channels control axonal action potential waveform and synaptic efficacy," Neuron **55**, 633–647 (2007).
42. M. B. Hoppa, G. Gouzer, M. Armbruster, *et al.*, "Control and plasticity of the presynaptic action potential waveform at small CNS nerve terminals," Neuron **84**, 778–789 (2014).
43. M. S. Scarnati, S. G. Clarke, Z. P. Pang, *et al.*, "Presynaptic calcium channel open probability and changes in calcium influx throughout the action potential determined using AP-waveforms," Front. Synaptic Neurosci. **12**, 17 (2020).
44. J. R. Geiger, J. Lübke, A. Roth, *et al.*, "Submillisecond AMPA receptor-mediated signaling at a principal neuron–interneuron synapse," Neuron **18**, 1009–1023 (1997).
45. M. Zbili, S. Rama, P. Yger, *et al.*, "Axonal Na^+ channels detect and transmit levels of input synchrony in local brain circuits," Sci. Adv. **6**, eaay4313 (2020).
46. D. Fricker and R. Miles, "EPSP amplification and the precision of spike timing in hippocampal neurons," Neuron **28**, 559–569 (2000).
47. G. Stuart and B. Sakmann, "Amplification of EPSPs by axosomatic sodium channels in neocortical pyramidal neurons," Neuron **15**, 1065–1076 (1995).
48. X. Chen, Z. Zeng, R. Li, *et al.*, "Superior performance with sCMOS over EMCCD in super-resolution optical fluctuation imaging," J. Biomed. Opt. **21**, 066007 (2016).
49. J. Liang, P. Wang, L. Zhu, *et al.*, "Single-shot stereo-polarimetric compressed ultrafast photography for light-speed observation of high-dimensional optical transients with picosecond resolution," Nat. Commun. **11**, 5252 (2020).
50. E. E. Thomson, M. Harfouche, K. Kim, *et al.*, "Gigapixel imaging with a novel multi-camera array microscope," eLife **11**, e74988 (2022).
51. K. C. Zhou, M. Harfouche, C. L. Cooke, *et al.*, "Parallelized computational 3D video microscopy of freely moving organisms at multiple gigapixels per second," Nat. Photonics **17**, 442–450 (2023).
52. Y.-L. Huang, A. S. Walker, and E. W. Miller, "A photostable silicon rhodamine platform for optical voltage sensing," J. Am. Chem. Soc. **137**, 10767–10776 (2015).